

Heterogeneities Shape Passive Intracellular Transport

Patrick Witzel,^{1,2} Maria Götz,^{1,2} Yann Lanoiselée,³ Thomas Franosch,⁴ Denis S. Grebenkov,³ and Doris Heinrich^{2,5,*}

¹Faculty for Chemistry and Pharmacy, Julius-Maximilians-Universität Würzburg, Würzburg, Germany; ²Fraunhofer Institute for Silicate Research ISC, Würzburg, Germany; ³Laboratoire de Physique de la Matière Condensée, CNRS-Ecole Polytechnique, Palaiseau, France;

⁴Institut für Theoretische Physik, Universität Innsbruck, Innsbruck, Austria; and ⁵Leiden Institute of Physics, Huygens-Kamerlingh Onnes Laboratory, Leiden University, Leiden, the Netherlands

ABSTRACT A living cell's interior is one of the most complex and intrinsically dynamic systems, providing an elaborate interplay between cytosolic crowding and ATP-driven motion that controls cellular functionality. Here, we investigated two distinct fundamental features of the merely passive, non-biomotor-shuttled material transport within the cytoplasm of *Dictyostelium discoideum* cells: the anomalous non-linear scaling of the mean-squared displacement of a 150-nm-diameter particle and non-Gaussian distribution of increments. Relying on single-particle tracking data of 320,000 data points, we performed a systematic analysis of four possible origins for non-Gaussian transport: 1) sample-based variability, 2) rarely occurring strong motion events, 3) ergodicity breaking/aging, and 4) spatiotemporal heterogeneities of the intracellular medium. After excluding the first three reasons, we investigated the remaining hypothesis of a heterogeneous cytoplasm as cause for non-Gaussian transport. A, to our knowledge, novel fit model with randomly distributed diffusivities implementing medium heterogeneities suits the experimental data. Strikingly, the non-Gaussian feature is independent of the cytoskeleton condition and lag time. This reveals that efficiency and consistency of passive intracellular transport and the related anomalous scaling of the mean-squared displacement are regulated by cytoskeleton components, whereas cytoplasmic heterogeneities are responsible for the generic, non-Gaussian distribution of increments.

INTRODUCTION

The dynamics of the cellular interior space comprise a sophisticated information and material transport, regulating and controlling cellular functionality and thus enabling homeostasis. The cytoplasm of a living cell is a highly dynamic and complex system consisting of the densely crowded cytosol (1), the organelles, and the structure-providing cytoskeleton components. Besides molecular diffusion on short ranges within the cytosol, vesicle transfer maintains macromolecular transport (2), immunological reaction, and signal transduction (3,4) and it provides nutrition. This transport consists of two distinct modes as vesicles undergo alternating phases of directed transport via motor proteins and diffusion-like motion within the cytosol (5–7). In the first case, three types of motor proteins are involved (8): kinesins and dyneins

travel along microtubules and allow for bidirectional transport toward the cell perimeter or the microtubule-organizing center (MTOC), respectively (9,10), whereas myosins move along the actin cortex (11–13). This so-called active or ATP-driven vesicle transport enables long-distance cargo delivery within the cell. Although our knowledge and understanding of this active vesicle transport have advanced a lot within the last decades, the diffusion-like motion of vesicles is still not well understood. Though the relevance of passive vesicle transport between active biomotor-driven phases is unquestioned—especially because of its general necessity for finding binding sites, binding to other cellular compartments, and enhancing of search strategies (14)—the experimental data basis in literature for these processes is scarce. Thus, we investigate this particular transport phenomenon via single-particle tracking of fluorescent 150-nm-diameter nanoparticles that mimic the dynamics of vesicles. With this diameter, we match the intermediate range of vesicles in most cell types and exceed the average actin mesh size of 100 nm (15), so particles do

Submitted January 11, 2019, and accepted for publication June 11, 2019.

*Correspondence: heinrich@physics.leidenuniv.nl

Patrick Witzel and Maria Götz contributed equally to this work.

Editor: Kinneret Keren.

<https://doi.org/10.1016/j.bpj.2019.06.009>

© 2019 Biophysical Society.



not enter the dense mesh located at the cell membrane and do not get stuck within. The particles exhibit no functional surface coating to prevent molecular motor binding and to ensure purely passive transport.

We utilized the cell system *Dictyostelium discoideum* (*D. discoideum*), a social amoeba, because of its similarities to mammalian cells regarding cell behavior, structure, and intracellular signaling, with a completely sequenced genome and a simple and basic cytoskeleton structure (16–19). *D. discoideum* serves as a relevant model organism for amoeboid migration (20,21), chemotaxis (22,23), phagocytosis, and human diseases (17,24). Of special interest for the investigations on intracellular processes is the truly three-dimensional (3D) shape of *D. discoideum* cells, which represents the natural morphology of cells in physiological 3D environments in the human body, in contrast to adherent, flat mammalian cells in conventional in vitro cell culture on flat surfaces (25). The cytoskeleton of *D. discoideum* cells is simple but comparable to mammalian cells and consists mainly of the actin cortex and microtubules, two biopolymers determining cell shape (see *upper left part of Fig. 1 A*). Whereas the actin cortex is a reorganizing network that is densest at the plasma membrane, the dynamically sweeping microtubules originate from the microtubule-organizing center MTOC adjacent to the nucleus, spreading toward the membrane and functioning as rails for intracellular transport by motor proteins (26,27). A relevant advantage of *D. discoideum* is the possibility to depolymerize these cytoskeleton components almost completely by drug treatment without causing cell death (see *Supporting Information*). Here, the drug latrunculin A prevents formation of the actin cortex by binding to the G-actin monomers (28); analogously, benomyl and nocodazole impede polymerization of the microtubule monomer tubulin (29,30). The injection of nanoparticles directly into the cytosol avoids their encapsulation by internal vesicles. Because these particles are functionally uncoated, they cannot bind to molecular motors (31) and thus uniquely witness the passive intracellular transport.

With this setup, we investigate two distinct fundamental aspects of the passive (not actively biomotor-shuttled) vesicle-like transport within the cytoplasm: the anomalous non-linear scaling of the mean-squared displacement (MSD) and the non-Gaussian distribution of its increments. Although the anomalous scaling and related subdiffusive and superdiffusive motions of various tracers in living cells have been thoroughly studied in the last 20 years (32–39), the non-Gaussian feature has only recently been experimentally discovered for subdiffusive motion of RNA-protein particles in live *Escherichia coli* and *Saccharomyces cerevisiae* cells (40). The observed exponential (Laplace) distribution was attributed to a combination of an exponential distribution in the time-averaged diffusivities and non-Gaussian behavior of individual trajectories due to significant heterogeneity

between trajectories and dynamic heterogeneity along single trajectories. Similar results were obtained for the acetylcholine receptors diffusing on live muscle-cell membranes (41). In turn, such features remain unknown for passive vesicle transport inside living cells because of the difficulty of acquiring enough sufficiently long trajectories of tracers in the living cell interior. Relying on a large amount of single-particle tracking data with, in total, 320,000 data points, we uncover the origin of non-Gaussian intracellular motion based on the analysis of increment probability densities, the ergodicity breaking parameter, and autocorrelation functions. We show that the cytoskeleton components—the actin cortex and the microtubules—control the efficiency of passive intracellular transport but not the non-Gaussian increment distributions. Unexpectedly, we find that a rescaling of the increment distributions by the mean absolute increment results in a collapse of all increment distributions onto one single master curve with an exponential tail. This master curve is independent of the cytoskeleton state and the lag time. We are able to assign the cause of non-Gaussian transport to spatiotemporal heterogeneities within the cytoplasm, opening new ways for future modeling of passive intracellular vesicle dynamics.

MATERIALS AND METHODS

Materials

$\text{Na}_2\text{HPO}_4 \cdot 2\text{H}_2\text{O}$ ($\geq 99.5\%$ p.a.; Carl Roth, Karlsruhe, Germany), KH_2PO_4 ($\geq 99\%$ p.a.; Carl Roth), D(+)-maltose monohydrate ($\geq 95\%$ p.a.; Carl Roth), latrunculin A (Thermo Fisher Scientific, Darmstadt, Germany), methyl 1-(butylcarbamoyl)-2-benzimidazolecarbamate (benomyl, 95%; Sigma-Aldrich, Taufkirchen, Germany), methyl N-(5-thienoyl-2-benzimidazolyl)carbamate (nocodazole, $\geq 99\%$; Sigma-Aldrich), gentamycin (G-418; Biochrom, Berlin, Germany), blasticidin (blasticidin S hydrochloride; Sigma-Aldrich), the cell culture medium HL5-C (ForMedium, Hunstanton, United Kingdom), and nanoscreenMAG-D particles (150 nm, polydispersion index 0.14–0.17; ChemiCell, Berlin, Germany) were used as received without further purification.

Cell culture

D. discoideum cells from the AX2 strain as wild type (WT), with LimE Δ cc-GFP expressed in LimE Δ cc-null and with α tubulin-GFP expressed in LimE Δ cc-mRFP were provided by Dr. Günther Gerisch (Max Planck Institute of Biochemistry, Martinsried, Germany). Cells were grown at 21°C in the cell culture medium HL5 adjusted to pH 6.7. For both the LimE Δ cc-GFP expressed in LimE Δ cc-null strain and the α tubulin-GFP expressed in LimE Δ cc-mRFP strain, the medium was complemented by the antibiotics gentamycin and blasticidin each at a concentration of 10 $\mu\text{g mL}^{-1}$. The cells were kept in the vegetative state at a confluence under 40%.

Experimental procedure

To avoid fluorescence of the medium, the cells were transferred to a non-fluorescent medium of 3.57 mM $\text{Na}_2\text{HPO}_4 \cdot 2\text{H}_2\text{O}$, 3.46 mM KH_2PO_4 , and 52.58 mM D(+)-maltose monohydrate in water, adjusted to pH 6.7, 2 h before the experiment was started. Subsequently, green fluorescent

nanoscreenMAG-D particles (a priori agitated by sonication for 10 min) with a diameter of 150 nm were added to the cell suspension at a final concentration of 0.36 mg mL⁻¹. These particles exhibit a magnetite core surrounded by a starch matrix and offer no binding sites to molecular motors like kinesins, dyneins, or myosins. To prevent transport of the particles in vesicles within the cytosol, ballistic injection was performed by centrifugation at 4,000 rotations per minute in four subsequent periods of

3, 4, 4, and 5 min duration, each followed by gentle agitation for 5 min. For imaging, the cells were settled in an eight-well plate with a glass bottom (ibidi, Martinsried, Germany). After a resting time of 30 min, allowing the cells to adhere to the ground, excess nanoparticles were removed by washing the cells for three times with non-fluorescent medium. The inhibition of the actin polymerization (noAct) was performed by adding latrunculin A to the cell suspension at a final concentration of 20 μ M 30 min before

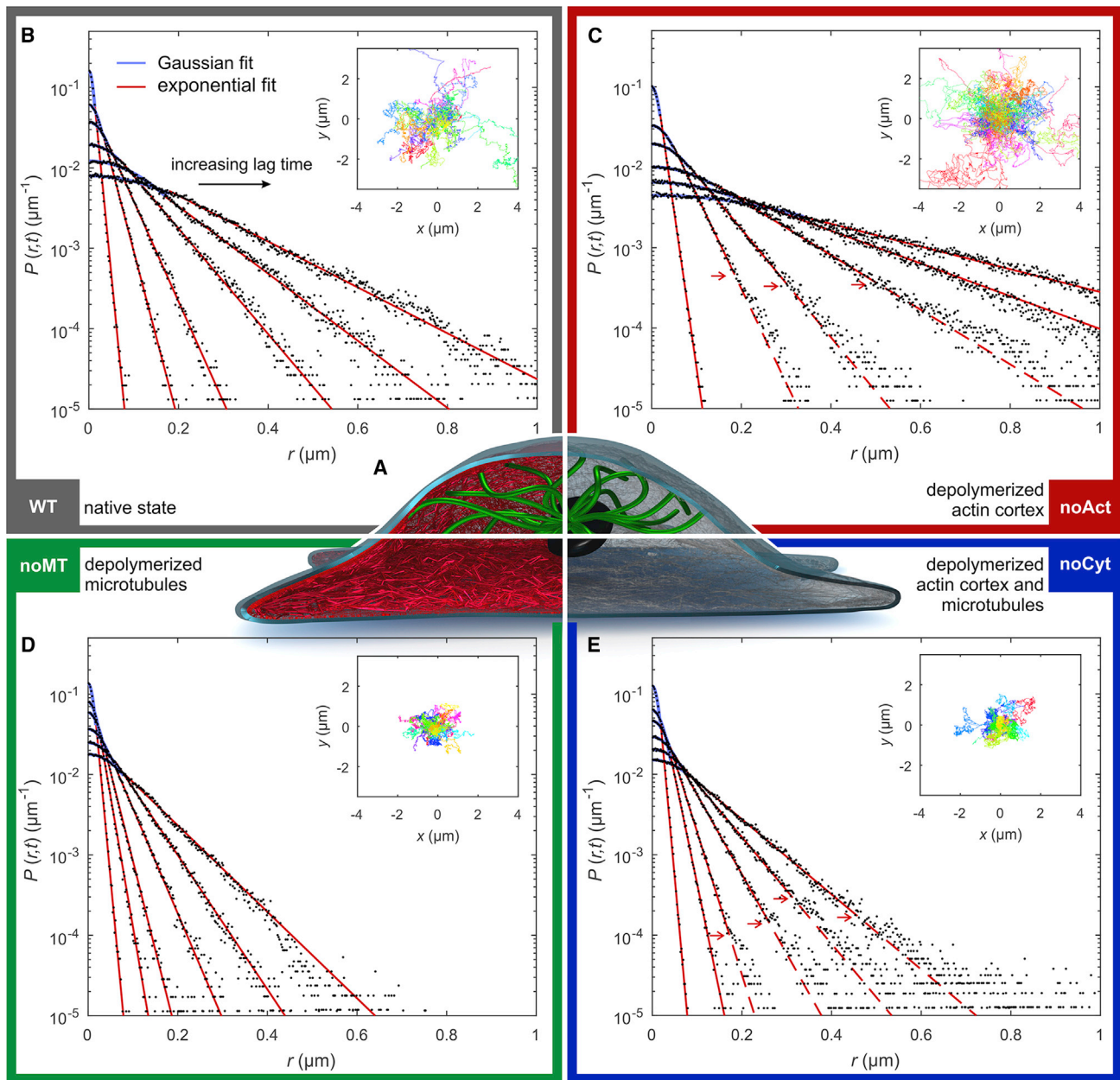


FIGURE 1 Increment probability densities of intracellular nanotracer trajectories for four different cytoskeleton states. (A) An illustration of a living eukaryotic cell exhibiting depolymerized cytoskeleton components (gray: cell membrane, black: nucleus, green: microtubule-organizing center (MTOC) with microtubules, red: actin cortex) is given. (B–E) Probability densities of absolute magnitudes of one-dimensional projected increments, $P(r, t)$, of intracellular nanotracers for lag times $t = \tau, 5\tau, 10\tau, 25\tau, 50\tau, 100\tau$ with the inverse frame rate $\tau = 49$ ms are given for four different cytoskeleton states: (B) wild type (WT), (C) depolymerized actin cortex (noAct), (D) depolymerized microtubules (noMT), and (E) depolymerized actin cortex and microtubules (noCyt); solid lines show the fit of a Gaussian function (light blue) followed by an exponential fit (red). For large lag times in the actin-deprived cases (noAct and noCyt), a deviation from the exponential fit (red) is indicated by dashed lines, and arrows show the transition point; (insets) all acquired trajectories of nanotracer motion are displayed in different colors, all starting from the origin (see details on the trajectories in the Supporting Information). To see this figure in color, go online.

the start of measurements (31). To prevent microtubule polymerization (noMT), the agents benomyl at a concentration of 50 μM and nocodazole at a concentration of 20 μM were mixed and added to the cells 30 min before the beginning of measurements (31). For the case without both microtubules and actin cortex (noCyt), latrunculin A, nocodazole, and benomyl were added to the cells 30 min before the experiments at the abovementioned concentrations. To monitor the drug efficiency, *D. discoideum* cells with LimE Δ cc-mRFP expressed in α tubulin-GFP have been treated equally at the same time. The fluorescent signals of GFP for the microtubules and RFP for Lim (a protein present at sites of freshly polymerized actin) vanished by treatment with benomyl, nocodazole, and latrunculin A or both, respectively. After removing the drugs by washing the cells with medium, the cells regenerated fully and showed normal behavior and cell division, with the fluorescent signals for both the Lim protein, indicating actin polymerization, and the microtubules visible again.

Microscopy

Live-cell imaging was performed on a Nikon eclipse Ti-E microscope (Nikon, Tokyo, Japan) equipped with an EM-CCD camera (C9100-50; Hamamatsu, Herrsching am Ammersee, Germany) using a 100 \times oil immersion objective with an NA of 1.4 (Nikon) and an additional inbuilt lens of 1.5 \times magnification yielding a resolution of 54 nm per pixel. An Intensilight (Nikon, Düsseldorf, Germany) and a filter set (F36 525 HC; AHF, Tübingen, Germany) with transmission wavelengths from 457 to 487 nm for excitation and transmission wavelengths from 500 to 540 nm for the detection path were utilized to image the fluorescent nanoparticles. These nanoparticles within *D. discoideum* cells were imaged every 49 ms, adjusting the focal plane manually with the acquisition software NIS-Elements AR at a 14-bit image depth. Imaging was performed at intermediate cell height, and the acquisition always took place close to the central cell plane and at similar distances from the nucleus and the outer cell periphery to keep locus-specific differences of the nanoparticle motion as small as possible. Particle tracking was performed by tracking software, OpenBox 1.64 (Informationssysteme Schilling, Germany), using two-dimensional Gaussian fits. This setup allows for a lateral tracking accuracy of ± 10 nm (42).

[Videos S1](#) and [S2](#) for the visualization of the cytoskeletal dynamics of LimE Δ cc-GFP expressed in LimE Δ cc-null and α tubulin-GFP expressed in LimE Δ cc-mRFP strains were acquired on a confocal microscope setup equipped with a spinning disk unit. The setup consists of an inverted microscope (Ti-E; Nikon), a spinning disk unit (UltraVIEW VoX; Perkin Elmer, Waltham, MA), a CCD camera (C9100-50; Hamamatsu), and two lasers (488 and 561 nm; Yokogawa Electric, Tokyo, Japan). The imaging was performed by a 100 \times immersion oil objective with an NA of 1.45 at a frame rate of 0.5 fps for [Video S1](#) and 10 fps for [Video S2](#). For acquisition, the software Volocity (Perkin Elmer) was used.

Statistical analysis

All statistical analyses are applied to the unchanged two-dimensional single-particle trajectories, i.e., the successive positions $\{(x_m(n\tau), y_m(n\tau)) | n = 1, \dots, N_m\}$ of the m -th tracer acquired at equal time intervals of duration τ (here, N_m is the number of points of the m -th trajectory). We are well aware of localization errors as well as the spurious correlation in the velocity autocorrelation function (VAF) appearing because of various measurement noises. Although advanced estimators can correct for some errors in case of Brownian motion (43–45), no generic correction protocol is available for a more general, anomalous, non-Gaussian motion as in this study. Moreover, because our goal is not the estimation of the scaling exponent but the analysis of the increment distributions, we keep using the genuine data sets to avoid eventual biases or artifacts.

The empirical probability density $P(r, t)$ of absolute magnitudes r of one-dimensional projected increments was evaluated at discrete points $r = k\rho$ (with a chosen bin size ρ) and $t = n\tau$ as $P(k\rho, n\tau) = p_k(n\tau)/\rho p(n\tau)$, where $p_k(t)$ is the number of times that the absolute one-dimensional increment $|x_m(q\tau + n\tau) - x_m(q\tau)|$ or $|y_m(q\tau + n\tau) - y_m(q\tau)|$ belongs to the interval $(k\rho, (k+1)\rho]$ and the normalization factor $p(n\tau)$ is the sum of all $p_k(n\tau)$. Here, one uses the increments for all tracers in a cytoskeleton state (i.e., $m = 1, \dots, M$) and for all possible shifts along each trajectory (i.e., $q = 1, \dots, N_m - n$). In other words, the probability density of increments includes the ensemble average over all trajectories in a state (e.g., the WT case) and the time average along each trajectory. The time average was crucial to improve the statistics of increments. For the same purpose, the increments along the X and Y coordinates were merged. From all trajectories in each of four cytoskeleton states ([Table S1](#)), we obtained 152,804, 160,958, 176,528, and 164,300 one-step increments for the WT, noAct, noMT, and noCyt cases, respectively. This large amount of data points is necessary for a sufficient signal/noise ratio of the increment probability density distributions and to average locus-specific variations of the particle motion. Based on these increments, histograms were produced for each cytoskeleton state and at different lag times t , from τ to 100τ .

In addition, the time-averaged VAF, characterizing correlations of one-step one-dimensional increments, was computed for each trajectory ($m = 1, \dots, M$) as

$$C_m(n\tau) = \frac{1}{2} \left(\frac{U_m^x(n)}{U_m^x(0)} + \frac{U_m^y(n)}{U_m^y(0)} \right), \quad (1)$$

where

$$U_m^x(n) = \frac{1}{N_m - n} \sum_{k=1}^{N_m-n} (x_m(k\tau) - x_m((k-1)\tau)) \times (x_m((k+n)\tau) - x_m((k+n-1)\tau))$$

is the time-averaged VAF of one-step increments along the X coordinate (similarly $U_m^y(n)$ for the Y coordinate), N_m is the number of points of the m -th trajectory, and n is the discrete lag time. Note also that

$$\sigma_m = \left(\frac{U_m^x(0) + U_m^y(0)}{2} \right)^{\frac{1}{2}} \quad (2)$$

is the empirical standard deviation (SD) of one-step one-dimensional increments ([Table S2](#)) that was used to obtain the rescaled probability densities.

The empirical histograms were fitted by a standard non-linear Levenberg-Marquardt least-squares algorithm in MATLAB (lsqcurvefit; The MathWorks, Natick, MA). Fitting was performed on a trustworthy region of the increment probability density distributions, defined by equal or more than 100 data points in the interval $(k\rho, (k+1)\rho]$.

The distributed model to fit the scale function $P(r, t)$ is derived in the [Supporting Information](#).

RESULTS AND DISCUSSION

Passive intracellular material transport was probed by single-particle-tracked tracers of a diameter of 150 nm. These nanoparticles (one per cell) have been injected directly into the cytosol of *D. discoideum* cells by centrifugation—not enclosed by vesicles—and thus reflect the passive dynamics of the cytoplasmic space exclusively. To elucidate the cytoplasm influence, *D. discoideum* cells were drug

treated for four different cytoskeleton states (**Fig. 1 A**): untreated WT, depolymerized microtubules (noMT), depolymerized actin cortex (noAct), and with disrupted cytoskeleton (noCyt) by a combination of polymerization-inhibiting drugs (see [Supporting Information](#)). For all experiments, cell-mediated, biomotor-regulated transport, e.g., along microtubules, has been effectively excluded by using particles that are unable to bind to cellular components. Based on more than 320,000 data points of nanoparticle trajectories (*insets* of **Fig. 1, B–E**; **Fig. S1**), we analyzed the probability densities of absolute magnitudes of one-dimensional projected increments for different lag times to gain a deeper insight into the cause for non-Gaussian intracellular transport.

Probability densities of nanoparticle displacement

For all four distinct cytoskeleton states, these probability densities (**Fig. 1, B–E**) exhibit an overall non-Gaussian behavior comprising a parabolic Gaussian-like region for small increments and an exponential tail for larger increments. This behavior is different from the exponential (Laplace) distribution without parabolic region, observed for the subdiffusive motion of RNA-protein particles ([40](#)). One difference between Gaussian and exponential distributions is that large increments are more likely to be realized in the latter case, which could lead to faster biochemical reactions within the cell. In both cases of actin deprivation (noAct, noCyt), further deviations from the exponential tail at even larger increments can be noticed (**Fig. 1, C and E**). Here, the dense actin network (see [Video S1](#)) is absent, leading to a broader increment distribution as compared to the WT state (**Fig. 1 B**) due to less-restricted particle motion (**Fig. 1 C**).

In contrast, single-particle tracking in cells lacking microtubules (noMT) yields less-spread trajectories (*inset* of **Fig. 1 D**), in which the corresponding probability densities (**Fig. 1 D**) behave similarly to those of the WT state yet at smaller increments. In the noMT state, the cell is set to a state of pure crowding because of the lack of the cytoplasm-fluidifying effect arising from the microtubules' sweeping motion (see [Video S2](#)). Depolymerizing the actin cortex and microtubules in the noCyt state combines these effects, obvious at longer lag times (**Fig. 1 E**): the cells lack both the confinement of the actin cortex and the active stirring of the microtubule motion. This results in a constrained particle motion as compared to the WT state but shows larger increments than in the noMT state, in which the additional confining effect of the actin cortex is present. This increment probability density analysis reveals the opposing functions of both cytoskeleton components in the cytoplasmic space of a living cell: whereas the actin cortex confines material transport within the cell interior, the actively driven dynamics of the microtubules fluidifies the

cytoplasm, fighting against intracellular crowding (see also the MSD in **Fig. 3 C** and discussion below).

Cause of non-Gaussian dynamics in passive intracellular transport

Material transport behavior with non-Gaussian increments has been observed and investigated in several non-living complex systems ([46–62](#)), ranging from glasses to granular matter and artificial F-actin networks, as well as for the dynamics of receptors on live cell membranes ([41](#)) and recently in living prokaryotic cell interiors ([63](#)) and in yeast ([40](#)). In those systems, non-Gaussian transport features have been rationalized by 1) sample-based variability, 2) rare occurring strong motion events, 3) aging, or 4) spatiotemporal heterogeneities of the medium. In the following, we investigate which of these reasons is applicable to the eukaryotic intracellular medium.

Sample-based variability

Non-Gaussian increment distributions across an ensemble of trajectories can be interpreted in two ways: 1) each trajectory exhibits normally distributed increments, whereas their diffusivity changes from one trajectory to another; or 2) the diffusivity changes along each trajectory. The validation of the Gaussian hypothesis for increments from each trajectory is restricted because of a limited length of individual trajectories, prohibiting an accurate computation of the probability density of increments for each single trajectory. For this reason, we resort to statistical tests of Gaussianity, which can be applied to individual trajectories. Among various statistical tests, we chose the Anderson-Darling and the Shapiro-Wilk tests, both shown to be the most efficient for testing Gaussianity on small samples ([64,65](#)). This analysis (see **Table S2**) reveals that non-Gaussian features are intrinsic to each trajectory. To reduce the general cell-related variability, all one-step increments of all trajectories were rescaled by dividing the one-step increments within each individual cell by their standard deviation (SD). **Fig. 2, A–C** shows the rescaled distributions for three lag times t : τ , 10τ , and 100τ , where $\tau = 49$ ms is the one-step duration, which represents the inverse frame rate. For all cytoskeleton states, the rescaled probability densities collapse to a single curve at the smallest lag time, whereas the curves are paired at a longer lag time of $t = 100\tau$: the WT and noAct states exhibit larger increments caused by the presence of the microtubules' sweeping motion, whereas the noMT and noCyt states show smaller increments arising from intracellular motion without the influence of microtubule dynamics. Furthermore, this rescaling eliminates deviations from the exponential tail at large increments (**Fig. 2, A–C**), which occurred exclusively in the noAct and noCyt states, both characterized by a depolymerized actin cortex (**Fig. 1, C and E**). Thus, the original deviations can be attributed to sample-based variability among individual cells,

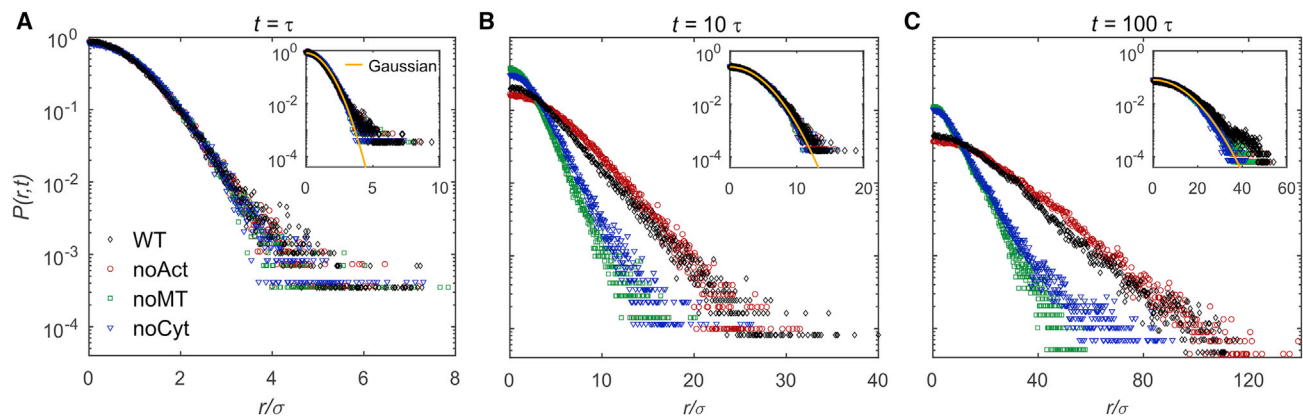


FIGURE 2 Increment probability densities of intracellular nanotracer trajectories rescaled by standard deviation (SD). Probability densities of increments for four cytoskeleton states (WT, noAct, noMT, noCyt) are shown for lag times $t = \tau$ (A), 10τ (B), and 100τ (C) with the inverse frame rate $\tau = 49$ ms; the one-step increments were rescaled by the SD σ for each individual cell. Insets show the increment probability densities for randomly shuffled, rescaled increments for lag times $t = \tau$ (inset A), 10τ (inset B), and 100τ (inset C) with the inverse frame rate $\tau = 49$ ms; the solid line shows the one-sided Gaussian distribution $2\exp(-r^2/2\sigma^2 t)/\sqrt{2\pi\sigma^2 t}$, with $\sigma = 1$ because of the rescaled increments (A and its inset are identical because shuffling of one-step increments does not affect their distribution). To see this figure in color, go online.

also evident from the larger spread of the one-step increment SDs between individual cells in both actin-deprived cases (noAct and noCyt) (see Tables S3 and S4). This elucidates the important role of the actin cortex as reducing the cell-to-cell heterogeneity of the cellular interior space for well-regulated, consistent transport dynamics across a cell population. At the same time, the persistence of an exponential tail in the rescaled data of all cytoskeleton states eliminates sample-based variability as a reason for non-Gaussian features in passive intracellular motion.

Rarely occurring strong motion events

Another cause for non-Gaussian increment distributions could be strong, rare events. In the cytosol, these can arise from nearby passing microtubules, intracellular cargo, or actin reorganization. For the cell state with both depolymerized microtubules and depolymerized actin cortex (noCyt), all active cytoskeleton dynamics within the cell have been eliminated, but the increment distribution still exhibits non-Gaussian behavior (Fig. 2, A–C, blue triangles). The existence of a non-Gaussian increment distribution with an exponential tail in the noCyt case—without any cytoskeleton components—is clear evidence against the second option of rarely occurring strong events.

Aging

Possible aging effects, i.e., non-vanishing dependence on initial conditions and progressive slowing down of the dynamics, can also lead to non-Gaussian transport. In fact, long stalling periods of a particle may render its increments at a fixed lag time highly heterogeneous and strongly correlated, breaking the applicability of the central limit theorem. These effects have been theoretically studied within a continuous-time random walk model (66), whereas the aging and ergodicity breaking of the receptor dynamics

on a cell membrane were recently reported (67,68). Aging effects can be characterized by the ergodicity breaking parameter (69,70), which describes fluctuations of the time-averaged MSD. As Fig. 3 A shows, the ergodicity breaking parameter vanishes with increasing experimental observation time, which corresponds to the length of trajectories, so that an aging effect can be excluded. Thus, the motion of 150 nm particles within the cytosol is ergodic at investigated timescales, and aging cannot account for non-Gaussian increment distributions (see Supporting Information).

Spatiotemporal heterogeneities of the medium

After excluding three possible reasons of non-Gaussian behavior within the intracellular medium, we now address the hypothesis of a spatiotemporal heterogeneous medium. Non-Gaussian distributions of increments are found for all considered lag times and all cytoskeleton states (Figs. 1 and 2). For lag time $t = \tau$, a possible reason for non-Gaussianity could be that one-step increments are not identically distributed. However, the distribution of large lag-time increments, which could be considered as the sum of numerous one-step increments, would be unavoidably Gaussian because of the central limit theorem (i.e., according to the Lindeberg condition) if the one-step increments were independent. To prove this non-independence, we perform a random reshuffling of one-step increments within each experimental trajectory to destroy all possible correlations (insets of Fig. 2). In all four cytoskeleton states, the reshuffled increment distributions become much closer to each other and to a Gaussian curve with moderate or minor deviations. The non-Gaussian character of the original (non-reshuffled) increment distributions at large lag times could thus be rationalized by the presence of strong, long-range correlations between

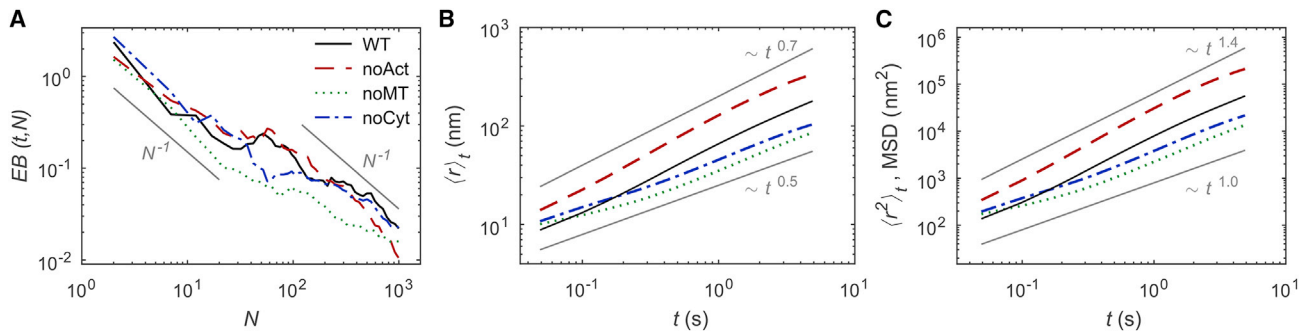


FIGURE 3 Ergodicity breaking parameter, mean absolute increment, and MSD for four cytoskeleton states (WT, noAct, noMT, and noCyt). (A) Ergodicity breaking parameter is shown as function of trajectory length N ; two indicative lines in gray show the typical $1/N$ decay for Brownian motion. (B) Mean absolute increments, $\langle r \rangle_t$, are shown as functions of lag time t for all cytoskeleton states; gray lines show two power laws: $t^{0.5}$ for diffusive and $t^{0.7}$ for super-diffusive motion. (C) MSDs, $\langle r^2 \rangle_t$, are shown as functions of lag time t for all cytoskeleton states; gray lines show two power laws: $t^{1.0}$ for diffusive and $t^{1.4}$ for superdiffusive motion. To see this figure in color, go online.

one-step increments. To verify this hypothesis, the velocity autocorrelation function (VAF) is evaluated, which reflects the temporal change in the magnitude and directionality of successive increments. The VAF reveals positive correlations over timescales of ~ 2 s only for the WT and the noAct cases (Fig. 4 A), which can thus be attributed to sweeping motion of microtubules (see Video S2). These correlations could be a possible reason for non-Gaussian increment distributions at large lag times, but only for these two cell states (WT and noAct). In the cases without microtubules (noMT and noCyt), only short-ranged, negative correlations on a sub-100-ms timescale are present and thus not sufficient to rationalize the observed non-Gaussian increment distributions in these cell states.

If the dynamics was Gaussian, the VAF would fully determine its correlation properties. In turn, for a non-Gaussian

process, the VAF essentially reflects correlations in the directions of increments but is only weakly sensitive to eventual correlations in the magnitudes of increments. We therefore analyze such higher-order correlations by introducing the variance autocorrelation function of squared increments (VarAF) (see Supporting Information; (71)). Fig. 4 B shows positive, slowly decreasing autocorrelation of squared increments for all cytoskeleton states. A plausible scenario for obtaining correlated squared increments is a change of the effective diffusivity along the nanoparticle trajectory, arising either by a slowly evolving environment around the tracer (71–76), by the exploration of a quasistatic but spatially heterogeneous cytoplasm (77,78), or by both. These two distinct scenarios correspond to random motion with either time- or space-dependent diffusion coefficients or again both. A direct experimental proof for

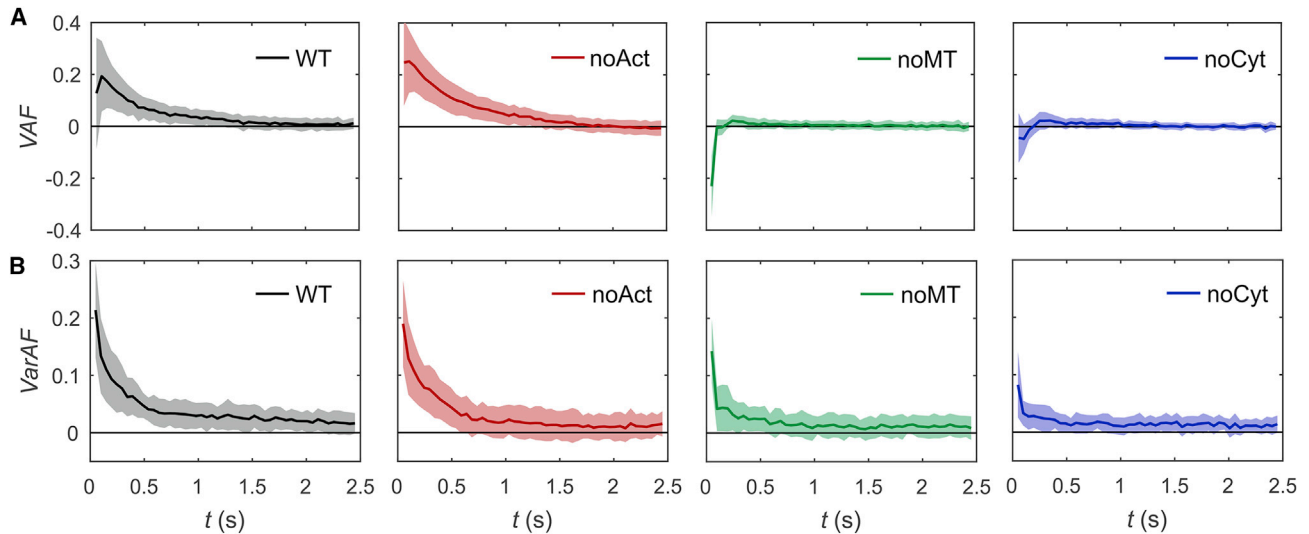


FIGURE 4 Velocity and variance autocorrelation functions. (A) Time-averaged velocity autocorrelation function (VAF) for four cytoskeleton states (WT, noAct, noMT, noCyt) are shown; solid lines correspond to the mean value obtained by averaging the velocity autocorrelations of all trajectories, and shaded areas mark the SD. (B) Time-averaged variance autocorrelation functions of squared increments (VarAF) for four cytoskeleton states (WT, noAct, noMT, noCyt) are shown; solid lines correspond to the mean value obtained by averaging the variance autocorrelations of all trajectories, and shaded areas mark the SD. To see this figure in color, go online.

heterogeneities causing non-Gaussian increment distributions within the cellular interior is beyond current state-of-the-art technology, especially in combination with the need for a large amount of data points. Our indirect experimental evidence of medium-induced spatiotemporal correlations, influencing intracellular transport, illustrates that the analysis of increment distributions provides deeper and more versatile insights into the intracellular dynamics in comparison to former studies based solely on MSD or velocity autocorrelations. When the cytoskeleton elements are progressively removed, the local diffusivity autocorrelations are getting lower, from the WT and noAct states to noMT and noCyt states. This qualitative observation agrees with the expected reduction of heterogeneities in these cytoskeleton states.

Generic character of passive intracellular transport

An additional rescaling of the n -step increments—already rescaled by the individual SD for every cell—was performed by the mean increment, $\langle r \rangle_t$, over all trajectories within a cytoskeleton state at lag time $t = n\tau$. This resulted in a superimposition of the probability densities for all cytoskeleton states and lag times onto one master curve (see Fig. 5 and Fig. S3 for each cytoskeleton state). Thus, these probability densities of magnitudes of increments exhibit a scaling form,

$$P(r, t) = \langle r \rangle_t^{-1} \hat{P}(\hat{r}), \quad \hat{r} = \frac{r}{\langle r \rangle_t}, \quad (3)$$

independent of the lag time t and independent of whether the motion is influenced by active cytoskeleton components—microtubules or actin cortex—or not. Note that the inverse increment $\langle r \rangle_t^{-1}$ in Eq. 3 accounts for the dimensionality

of the probability density. Residual deviations from the master curve appear at large increments when the probability density is small and thus characterizes relatively rare moves. These deviations are stronger for the noCyt case at $t = 100\tau$, which might be related to larger heterogeneity due to the lack of actin. The scaling form (Eq. 3) clearly indicates a generic intracellular dynamics feature, which is independent of the cytoskeleton components in *D. discoideum* cells for the 150-nm-diameter particles used and for lag times up to 4.9 s. Based on this scaling behavior, the transition of the increment probability distributions from a Gaussian-like regime to an exponential tail is an intrinsic property of the underlying intracellular material transport, and the shape of the probability density is captured solely by the master curve \hat{P} . Thus, microtubules and the actin cortex do not change the increment distribution, which is controlled by heterogeneities, but regulate the efficiency of the intracellular dynamics like a gear shift mechanism, enabling well-controlled intracellular material and information transport.

Two-parameter model

To gain insight into the behavior of the master curve \hat{P} , we propose a distributed model of Gaussian increments with random SDs σ exhibiting only two parameters. An explicit form of the master curve \hat{P} is deduced (see Supporting Information for more details) from the assumed χ distribution for σ :

$$\hat{P}(\hat{r}) = \frac{\alpha(\alpha\hat{r})^{\nu-\frac{1}{2}} K_{\nu-\frac{1}{2}}(\alpha\hat{r})}{\sqrt{\pi} 2^{\nu-\frac{3}{2}} \Gamma(\nu)}, \quad \alpha = \frac{2 \Gamma(\nu + \frac{1}{2})}{\sqrt{\pi} \Gamma(\nu)}, \quad (4)$$

where $K_{\nu-\frac{1}{2}}$ is the modified Bessel function of the second kind, $\Gamma(\nu)$ denotes the Gamma function, and the shape

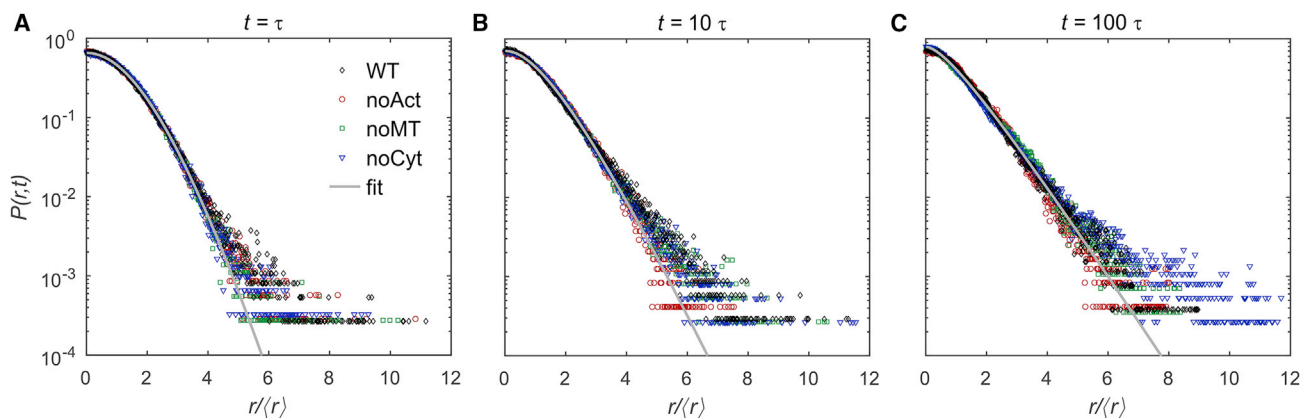


FIGURE 5 Increment probability densities of intracellular nanotracer trajectories rescaled by mean increments. (A) Probability densities of increments for four cytoskeleton states (WT, noAct, noMT, noCyt) are shown for lag times $t = \tau$ (A), 10τ (B), and 100τ (C) with the inverse frame rate $\tau = 49$ ms, with additional rescaling of the n -step increments by their mean absolute increments $\langle r \rangle_t$ at lag time $t = n\tau$ for each cytoskeleton state; solid lines show a representative fit by Eqs. 3 and 4 for the noMT case. Fits for the three other cases are overlapping and therefore not shown. The values of the shape parameter ν are 3.5 (A), 3.4 (B), and 1.8 (C); see also Fig. S3 for the dependence of ν on the lag time for all four cytoskeleton states. To see this figure in color, go online.

parameter ν quantifies the spread of SDs σ . At the particular value $\nu = 1$, our model yields the one-sided exponential (Laplace) distribution, $\hat{P}(\hat{r}) = \exp(-\hat{r})/2$, observed in other experiments (40). The shape parameter $\nu > 1$ is needed to reproduce a parabolic region at small increments observed in our experiments. The second parameter is the scale of increments, $\langle r \rangle_t$, which incorporates the scaling with the lag time. The resulting probability density $P(r, t)$ reproduces both the Gaussian-like regime at small increments and the exponential tail at large increments, in perfect agreement with experimental data for all cytoskeleton states and all lag times (Fig. 5).

The collapse of all increment probability densities onto a single master curve implies that the dynamics-related differences between the four cytoskeleton states are captured solely by the mean absolute increment $\langle r \rangle_t$. Fig. 3 shows $\langle r \rangle_t$ as well as the closely related MSD $\langle r^2 \rangle_t$ (Fig. 3, B and C, respectively), as a function of the lag time t . In cases without microtubules (noMT and noCyt cases), one observes a linear scaling of the MSD, $\langle r^2 \rangle_t \propto t$ for larger lag times, whereas initial subdiffusive regimes are present with $\langle r^2 \rangle_t \propto t^{0.6}$ up to 0.1 s for the cytoskeleton state without microtubules (noMT) and with $\langle r^2 \rangle_t \propto t^{0.9}$ up to a lag time of 0.3 s in cells with depolymerized cytoskeleton (noCyt). We emphasize that super- or subdiffusive scaling of the MSD with the lag time and the non-Gaussian character of the increment distribution are distinct features. For instance, fractional Brownian motion exhibits Gaussian increments while its MSD scales as a power law, whereas many diffusing diffusivity processes (72–75) exhibit non-Gaussian increments with a linear scaling of the MSD. Diffusion in such a passive crowded heterogeneous medium was formerly observed in non-living systems and called “anomalous (non-Gaussian) yet Brownian motion” (54,55), and the transition from subdiffusive regimes to normal diffusion with increasing lag time is commonly known (79,80). In contrast, the sweeping motion of microtubules creates local flows in the cytoplasm and results in a superdiffusive scaling in WT and noAct cases, $\langle r^2 \rangle_t \propto t^\alpha$, with an exponent $\alpha \approx 1.4$. Although the superdiffusive motion of tracers in living cells was often observed (9,25,79–82), it was attributed to active biomotor-driven transport along microtubules. In our experiment, the mechanism is different. Moreover, we reveal for the first time, to our knowledge, both superdiffusive and non-Gaussian features of the passive intracellular transport in eukaryotic cells. Most importantly, we identify and decouple the origins of these fundamental aspects of intracellular dynamics.

CONCLUSIONS

In conclusion, the analysis of increment probability densities and autocorrelation functions reveals 1) the important role of the actin network reducing cell-to-cell heterogeneities and thus unifying intracellular material transport;

2) spatiotemporal heterogeneities as the reason for non-Gaussian transport features in living cells; and 3) a scaling of the increment probability densities independent of the cytoskeleton state for 150-nm-diameter nanoparticles, mimicking the passive vesicle motion, within the observed experiment time. In this respect, the presence of the exponential tail for all four cytoskeleton states and the scaling of all increment probability density functions indicate a ubiquitous dynamic feature of intracellular material transport in the cytoplasm, independent of the cytoskeleton components present in the cell. These, in contrast, are responsible for regulating the efficiency of intracellular motion. Additionally, the investigated anomalous transport features reflect the heterogeneities within the cytoplasm and their spatiotemporal changes. These results pave the way for experimental investigation and theoretical analysis of intracellular material transport features based on spatiotemporal medium fluctuations, enabling future insights in cellular mechanisms.

SUPPORTING MATERIAL

Supporting Material can be found online at <https://doi.org/10.1016/j.bpj.2019.06.009>.

AUTHOR CONTRIBUTIONS

D.H. and T.F. designed research. M.G. performed the experiments. P.W., Y.L., and D.S.G. analyzed data. P.W., M.G., D.S.G., and D.H. wrote the manuscript. All authors discussed the results and commented on the manuscript.

ACKNOWLEDGMENTS

P.W., M.G., and D.H. acknowledge Prof. Dr. Günther Gerisch (Max Planck Institute for Biochemistry, Germany) for providing the *D. discoideum* strains; P.W., M.G., and D.H. acknowledge funding from the Deutsche Forschungsgemeinschaft (grant HE5958-2-1), the Volkswagen-Foundation (grant I85100), and the Fraunhofer Gesellschaft for the Fraunhofer Attract grant “3DNanoCell”; D.S.G. and Y.L. acknowledge the support of the French National Research Agency (Grant No. ANR-13-JSV5-0006-01).

REFERENCES

- Ellis, R. J. 2001. Macromolecular crowding: an important but neglected aspect of the intracellular environment. *Curr. Opin. Struct. Biol.* 11:114–119.
- Tokarev, A. A., A. Alfonso, and N. Segev. 2009. Overview of intracellular compartments and trafficking pathways. In *Trafficking Inside Cells. Pathways, Mechanisms and Regulation*. N. Segev, ed. Springer, pp. 3–14.
- Neuhäus, E. M., W. Almers, and T. Soldati. 2002. Morphology and dynamics of the endocytic pathway in *Dictyostelium discoideum*. *Mol. Biol. Cell.* 13:1390–1407.
- Spang, A. 2008. The life cycle of a transport vesicle. *Cell. Mol. Life Sci.* 65:2781–2789.
- Hafner, A. E., L. Santen, ..., M. R. Shaebani. 2016. Run-and-pause dynamics of cytoskeletal motor proteins. *Sci. Rep.* 6:37162.

6. Brangwynne, C. P., G. H. Koenderink, ..., D. A. Weitz. 2009. Intracellular transport by active diffusion. *Trends Cell Biol.* 19:423–427.
7. Goychuk, I., V. O. Kharchenko, and R. Metzler. 2014. How molecular motors work in the crowded environment of living cells: coexistence and efficiency of normal and anomalous transport. *PLoS One.* 9:e91700.
8. Schliwa, M., and G. Woehlke. 2003. Molecular motors. *Nature.* 422:759–765.
9. Appert-Rolland, C., M. Ebbinghaus, and L. Santen. 2015. Intracellular transport driven by cytoskeletal motors. General mechanisms and defects. *Phys. Rep.* 593:1–59.
10. Sackmann, E., F. Keber, and D. Heinrich. 2010. Physics of cellular movements. *Annu. Rev. Condens. Matter Phys.* 1:257–276.
11. Vale, R. D. 2003. The molecular motor toolbox for intracellular transport. *Cell.* 112:467–480.
12. Schuh, M. 2011. An actin-dependent mechanism for long-range vesicle transport. *Nat. Cell Biol.* 13:1431–1436.
13. Snider, J., F. Lin, ..., S. P. Gross. 2004. Intracellular actin-based transport: how far you go depends on how often you switch. *Proc. Natl. Acad. Sci. USA.* 101:13204–13209.
14. Bénichou, O., C. Loverdo, ..., R. Voituriez. 2011. Intermittent search strategies. *Rev. Mod. Phys.* 83:81–129.
15. Morone, N., T. Fujiwara, ..., A. Kusumi. 2006. Three-dimensional reconstruction of the membrane skeleton at the plasma membrane interface by electron tomography. *J. Cell Biol.* 174:851–862.
16. Maniak, M. 2011. Dictyostelium as a model for human lysosomal and trafficking diseases. *Semin. Cell Dev. Biol.* 22:114–119.
17. Annesley, S. J., and P. R. Fisher. 2009. Dictyostelium discoideum—a model for many reasons. *Mol. Cell. Biochem.* 329:73–91.
18. Williams, J. G. 2010. Dictyostelium finds new roles to model. *Genetics.* 185:717–726.
19. Williams, R. S., K. Boeckeler, ..., S. Alexander. 2006. Towards a molecular understanding of human diseases using Dictyostelium discoideum. *Trends Mol. Med.* 12:415–424.
20. Wolf, K., R. Müller, ..., P. Friedl. 2003. Amoeboid shape change and contact guidance: T-lymphocyte crawling through fibrillar collagen is independent of matrix remodeling by MMPs and other proteases. *Blood.* 102:3262–3269.
21. L. Eichinger and F. Rivero, eds 2013. Dictyostelium discoideum Protocols, Second edition Humana Press, Totowa, NJ.
22. Meier, B., A. Zielinski, ..., D. Heinrich. 2011. Chemotactic cell trapping in controlled alternating gradient fields. *Proc. Natl. Acad. Sci. USA.* 108:11417–11422.
23. Nichols, J. M., D. Veltman, and R. R. Kay. 2015. Chemotaxis of a model organism: progress with Dictyostelium. *Curr. Opin. Cell Biol.* 36:7–12.
24. Müller-Taubenberger, A., A. Kortholt, and L. Eichinger. 2013. Simple system–substantial share: the use of Dictyostelium in cell biology and molecular medicine. *Eur. J. Cell Biol.* 92:45–53.
25. Dupont, A., M. Gorelashvili, ..., D. Heinrich. 2013. Three-dimensional single-particle tracking in live cells: news from the third dimension. *New J. Phys.* 15:75008.
26. Fletcher, D. A., and R. D. Mullins. 2010. Cell mechanics and the cytoskeleton. *Nature.* 463:485–492.
27. Alberts, B. 2015. Molecular Biology of the Cell. Garland Science, Taylor and Francis Group, New York, NY.
28. Morton, W. M., K. R. Ayscough, and P. J. McLaughlin. 2000. Latrunculin alters the actin-monomer subunit interface to prevent polymerization. *Nat. Cell Biol.* 2:376–378.
29. Peterson, J. R., and T. J. Mitchison. 2002. Small molecules, big impact: a history of chemical inhibitors and the cytoskeleton. *Chem. Biol.* 9:1275–1285.
30. Zhou, Y., J. Xu, ..., M. Zhou. 2016. Mechanism of action of the benzimidazole fungicide on *Fusarium graminearum*: interfering with polymerization of monomeric tubulin but not polymerized microtubule. *Phytopathology.* 106:807–813.
31. Otten, M., A. Nandi, ..., D. Heinrich. 2012. Local motion analysis reveals impact of the dynamic cytoskeleton on intracellular subdiffusion. *Biophys. J.* 102:758–767.
32. Tolić-Nørrelykke, I. M., E. L. Munteanu, ..., K. Berg-Sørensen. 2004. Anomalous diffusion in living yeast cells. *Phys. Rev. Lett.* 93:078102.
33. Golding, I., and E. C. Cox. 2006. Physical nature of bacterial cytoplasm. *Phys. Rev. Lett.* 96:098102.
34. Jeon, J. H., V. Tejedor, ..., R. Metzler. 2011. In vivo anomalous diffusion and weak ergodicity breaking of lipid granules. *Phys. Rev. Lett.* 106:048103.
35. Bertseva, E., D. Grebenkov, ..., L. Forró. 2012. Optical trapping micro rheology in cultured human cells. *Eur. Phys. J. E.* 35:63.
36. Höfling, F., and T. Franosch. 2013. Anomalous transport in the crowded world of biological cells. *Rep. Prog. Phys.* 76:046602.
37. Di Renzo, C., V. Piazza, ..., F. Cardarelli. 2014. Probing short-range protein Brownian motion in the cytoplasm of living cells. *Nat. Commun.* 5:5891.
38. Etoc, F., E. Balloul, ..., M. Coppey. 2018. Non-specific interactions govern cytosolic diffusion of nanosized objects in mammalian cells. *Nat. Mater.* 17:740–746.
39. Gal, N., and D. Weishs. 2010. Experimental evidence of strong anomalous diffusion in living cells. *Phys. Rev. E.* 81:020903.
40. Lampo, T. J., S. Stylianidou, ..., A. J. Spakowitz. 2017. Cytoplasmic RNA-protein particles exhibit non-Gaussian subdiffusive behavior. *Biophys. J.* 112:532–542.
41. He, W., H. Song, ..., P. Tong. 2016. Dynamic heterogeneity and non-Gaussian statistics for acetylcholine receptors on live cell membrane. *Nat. Commun.* 7:11701.
42. Mahowald, J., D. Arcizet, and D. Heinrich. 2009. Impact of external stimuli and cell micro-architecture on intracellular transport states. *ChemPhysChem.* 10:1559–1566.
43. Michalet, X., and A. J. Berglund. 2012. Optimal diffusion coefficient estimation in single-particle tracking. *Phys. Rev. E.* 85:061916.
44. Vestergaard, C. L., P. C. Blainey, and H. Flyvbjerg. 2014. Optimal estimation of diffusion coefficients from single-particle trajectories. *Phys. Rev. E.* 89:022726.
45. Kepten, E., I. Bronshtein, and Y. Garini. 2013. Improved estimation of anomalous diffusion exponents in single-particle tracking experiments. *Phys. Rev. E.* 87:052713.
46. Chaudhuri, P., L. Berthier, and W. Kob. 2007. Universal nature of particle displacements close to glass and jamming transitions. *Phys. Rev. Lett.* 99:060604.
47. Rouyer, F., and N. Menon. 2000. Velocity fluctuations in a homogeneous 2D granular gas in steady state. *Phys. Rev. Lett.* 85:3676–3679.
48. Orpe, A. V., and A. Kudrolli. 2007. Velocity correlations in dense granular flows observed with internal imaging. *Phys. Rev. Lett.* 98:238001.
49. Gollub, J. P., J. Clarke, ..., O. N. Mesquita. 1991. Fluctuations and transport in a stirred fluid with a mean gradient. *Phys. Rev. Lett.* 67:3507–3510.
50. Bertrand, O. J., D. K. Fygenson, and O. A. Saleh. 2012. Active, motor-driven mechanics in a DNA gel. *Proc. Natl. Acad. Sci. USA.* 109:17342–17347.
51. Stuhrmann, B., M. Soares E Silva, ..., G. H. Koenderink. 2012. Nonequilibrium fluctuations of a remodeling in vitro cytoskeleton. *Phys. Rev. E Stat. Nonlin. Soft Matter Phys.* 86:020901.
52. Toyota, T., D. A. Head, ..., D. Mizuno. 2011. Non-Gaussian athermal fluctuations in active gels. *Soft Matter.* 7:3234–3239.
53. Palacci, J., C. Cottin-Bizonne, ..., L. Bocquet. 2010. Sedimentation and effective temperature of active colloidal suspensions. *Phys. Rev. Lett.* 105:088304.

54. Wang, B., J. Kuo, ..., S. Granick. 2012. When Brownian diffusion is not Gaussian. *Nat. Mater.* 11:481–485.
55. Wang, B., S. M. Anthony, ..., S. Granick. 2009. Anomalous yet Brownian. *Proc. Natl. Acad. Sci. USA.* 106:15160–15164.
56. Leptos, K. C., J. S. Guasto, ..., R. E. Goldstein. 2009. Dynamics of enhanced tracer diffusion in suspensions of swimming eukaryotic microorganisms. *Phys. Rev. Lett.* 103:198103.
57. Scholz, M., S. Burov, ..., A. R. Dinner. 2016. Cycling state that can lead to glassy dynamics in intracellular transport. *Phys. Rev. X.* 6:011037.
58. Ghosh, S. K., A. G. Cherstvy, ..., R. Metzler. 2016. Anomalous, non-Gaussian tracer diffusion in crowded two-dimensional environments. *New J. Phys.* 18:13027.
59. Cherstvy, A. G., and R. Metzler. 2015. Ergodicity breaking and particle spreading in noisy heterogeneous diffusion processes. *J. Chem. Phys.* 142:144105.
60. Kahana, A., G. Kenan, ..., R. Granek. 2008. Active transport on disordered microtubule networks: the generalized random velocity model. *Phys. Rev. E.* 78:051912.
61. Moschakis, T., A. Lazaridou, and C. G. Biliaderis. 2012. Using particle tracking to probe the local dynamics of barley β -glucan solutions upon gelation. *J. Colloid Interface Sci.* 375:50–59.
62. Grady, M. E., E. Parrish, ..., D. M. Eckmann. 2017. Intracellular nanoparticle dynamics affected by cytoskeletal integrity. *Soft Matter.* 13:1873–1880.
63. Parry, B. R., I. V. Surovtsev, ..., C. Jacobs-Wagner. 2014. The bacterial cytoplasm has glass-like properties and is fluidized by metabolic activity. *Cell.* 156:183–194.
64. Shapiro, S. S., and M. B. Wilk. 1965. An analysis of variance test for normality (complete samples). *Biometrika.* 52:591–611.
65. Razali, N. M., and Y. B. Wah. 2011. Power comparisons of Shapiro-Wilk, Kolmogorov-Smirnov, Lilliefors and Anderson-Darling tests. *J. Stat. Model. Anal.* 2:21–33.
66. Metzler, R., and J. Klafter. 2000. The random walk's guide to anomalous diffusion: A fractional dynamics approach. *Phys. Rep.* 339:1–77.
67. Weigel, A. V., B. Simon, ..., D. Krapf. 2011. Ergodic and nonergodic processes coexist in the plasma membrane as observed by single-molecule tracking. *Proc. Natl. Acad. Sci. USA.* 108:6438–6443.
68. Manzo, C., J. A. Torreno-Pina, ..., M. F. Garcia Parajo. 2015. Weak ergodicity breaking of receptor motion in living cells stemming from random diffusivity. *Phys. Rev. X.* 5:11021.
69. He, Y., S. Burov, ..., E. Barkai. 2008. Random time-scale invariant diffusion and transport coefficients. *Phys. Rev. Lett.* 101:058101.
70. Burov, S., J. H. Jeon, ..., E. Barkai. 2011. Single particle tracking in systems showing anomalous diffusion: the role of weak ergodicity breaking. *Phys. Chem. Chem. Phys.* 13:1800–1812.
71. Lanoiselée, Y., and D. S. Grebenkov. 2018. A model of non-Gaussian diffusion in heterogeneous media. *J. Phys. A Math. Theor.* 51:145602.
72. Jain, R., and K. L. Sebastian. 2016. Diffusion in a crowded, rearranging environment. *J. Phys. Chem. B.* 120:3988–3992.
73. Chechkin, A. V., F. Seno, ..., I. M. Sokolov. 2017. Brownian yet non-Gaussian diffusion: from superstatistics to subordination of diffusing diffusivities. *Phys. Rev. X.* 7:530.
74. Lanoiselée, Y., N. Moutal, and D. S. Grebenkov. 2018. Diffusion-limited reactions in dynamic heterogeneous media. *Nat. Commun.* 9:4398.
75. Miyaguchi, T., T. Akimoto, and E. Yamamoto. 2016. Langevin equation with fluctuating diffusivity: a two-state model. *Phys. Rev. E.* 94:012109.
76. Chubynsky, M. V., and G. W. Slater. 2014. Diffusing diffusivity: a model for anomalous, yet Brownian, diffusion. *Phys. Rev. Lett.* 113:098302.
77. Hughes, B. D. 1995. Random Walks and Random Environments. Clarendon Press, Oxford.
78. Cherstvy, A. G., A. V. Chechkin, and R. Metzler. 2013. Anomalous diffusion and ergodicity breaking in heterogeneous diffusion processes. *New J. Phys.* 15:83039.
79. Tabei, S. M., S. Burov, ..., N. F. Scherer. 2013. Intracellular transport of insulin granules is a subordinated random walk. *Proc. Natl. Acad. Sci. USA.* 110:4911–4916.
80. Fakhri, N., A. D. Wessel, ..., C. F. Schmidt. 2014. High-resolution mapping of intracellular fluctuations using carbon nanotubes. *Science.* 344:1031–1035.
81. Caspi, A., R. Granek, and M. Elbaum. 2000. Enhanced diffusion in active intracellular transport. *Phys. Rev. Lett.* 85:5655–5658.
82. Reverey, J. F., J. H. Jeon, ..., C. Selhuber-Unkel. 2015. Superdiffusion dominates intracellular particle motion in the supercrowded cytoplasm of pathogenic Acanthamoeba castellanii. *Sci. Rep.* 5:11690.